The spin-singlet states in the double trellis-layer bronzes Na$_{0.56}$V$_2$O$_5$ with a uniform valence and Sr$_{0.5}$V$_2$O$_5$ with a valence order

The spin-singlet states in the double trellis-layer bronzes $Na_{0.56}V_2O_5$ with a uniform valence and $Sr_{0.5}V_2O_5$ with a valence order

Masashige Onoda and Junichi Hasegawa

Institute of Physics, University of Tsukuba, Tennodai, Tsukuba 305-8571, Japan

E-mail: onoda@sakura.cc.tsukuba.ac.jp

Abstract
The structural, transport and magnetic properties of the δ-phase bronzes $Na_{0.56}V_2O_5$ and $Sr_{0.5}V_2O_5$ with double trellis layers have been explored by means of x-ray diffraction and through measurements of electrical resistivity, thermoelectric power, magnetization and electron spin resonance. The properties of the Na compound with a uniform valence depend on the cooling rate likely due to the configuration for the order of Na: the slow cooling condition gives rise to a thermal hysteresis for the semiconducting transport and the spin-singlet state due to the large exchange coupling for the rung in the trellis layer. On the other hand, fast cooling leads to the absence of hysteresis and the metastable spin state depending on the measurement time. The Sr compound with a valence order close to V^{4+} and V^{5+} is insulating due to electron correlation, and it exhibits the singlet state originating from the alternating-exchange chain effect.

1. Introduction

Transition-metal oxides and ternary oxide bronzes with partially filled d-band have been investigated intensively to understand the basic properties of correlated-electron, electron–phonon-coupling and quantum spin-fluctuation systems, and to search for novel phenomena and functions.

Various low-dimensional spin networks exist in the vanadium oxide system. In this system, the half-filled insulator series CaV_nO_{2n+1} ($n = 2$–4) with two-dimensional $S = \frac{1}{2}$ networks at the V^{4+} site [1–3] has attracted much attention. For $n = 2$, a spin-singlet state appears basically due to dimerization for the next-neighbouring V pairs or the rung in a trellis layer that has three kinds of exchange coupling for the corner-shared leg (J) and rung (J') paths, and the edge-shared zigzag (J'') one [3, 4]. For $n = 4$, a singlet state originating from weakly coupled metaplaquettes is formed [5, 6]. On the other hand, for $n = 3$, a stripe-phase magnetic order
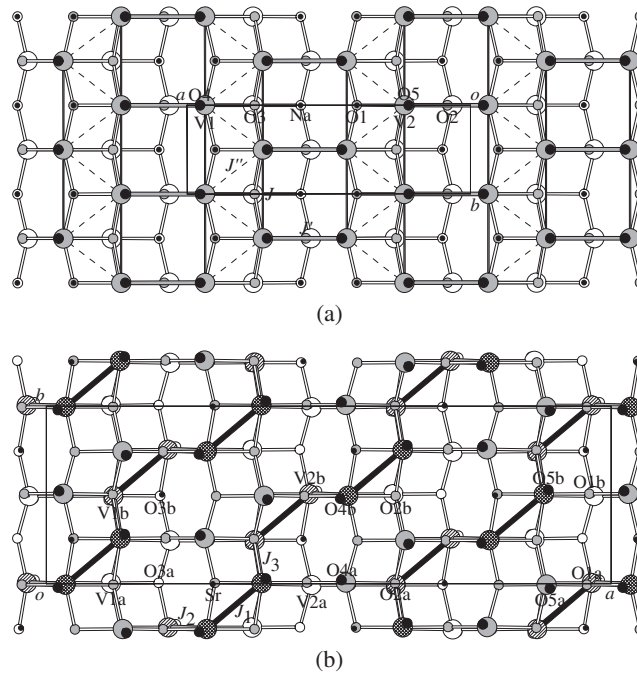
Figure 1. The crystal structures of (a) $Na_{0.56}V_2O_5$ and (b) $Sr_{0.5}V_2O_5$ projected on the ab-plane after [20, 21]. In (a) the open, shaded and full circles denote positions at $z = -0.17$ to -0.14, 0.10 to 0.17 and 0.35 to 0.52, respectively; and the thick and dotted lines indicate the V–V path at $z \simeq 0.166$, where J and J' express the superexchange couplings for the corner-sharing paths and J'' is for the edge-sharing path. In (b) the open, shaded and full circles are for $z = 0.34$–0.38, 0.59–0.66 and 0.84–1.01; and the hatched and cross-hatched ones connected with the thick lines show V^{4+}-like sites at $z \simeq 0.34$ and 0.66, where J_1 indicates the exchange coupling for the V1b–V2b path in the intralayer, and J_2 and J_3 are for the V2b–V2b and V1b–V1b paths in the interlayers, respectively.

takes place [7], and its origin is understood in terms of high-temperature series expansion [8]. The quarter-filled insulator NaV_2O_5, which has a structure similar to that of CaV_2O_5 [3, 9–11], shows one-dimensional $S = \frac{1}{2}$ magnetic properties with spins attached to a V–O–V molecular orbital [9, 12] and undergoes a transition to the singlet state [13] with a lattice distortion and a valence order [14]. The crossover between the spin-gap and the linear-chain properties as a function of band filling through the $Ca_{1-x}Na_xV_2O_5$ system was also explored [15].

The δ-phase vanadium bronze $M_xV_2O_5$, where M is a monovalent or divalent nonmagnetic ion and the x range depends on the species of M, has a double trellis layer with in-plane wavefunctions for the V ions. The structural and electronic properties of $Ag_xV_2O_5$ with $0.65 \leqslant x \leqslant 0.90$ and $Tl_xV_2O_5$ with $0.47 \leqslant x \leqslant 0.496$ were investigated by the authors' group [16, 17]. In the Ag system, the band filling can be varied greatly. The structure for $x = 0.68$ indicates that two crystallographically independent V ions in the double trellis layer have valences close to the average value expected from the chemical formula and the Ag ions have a site randomness. For $0.65 \leqslant x \leqslant 0.75$, first-order phase transitions with structural, transport and magnetic anomalies appear at $T_{c1} \simeq 220$ K. Below this temperature, accompanied with significant reduction of superexchange coupling constants, a nearly $\frac{1}{6}$-filled compound becomes spin-singlet originated from the trellis-layer model [18] with $J = 47$, $J' = 193$

and $J'' = 108$ K for[1] each coupling shown in figure 1(a), and other compositions remain paramagnetic. For $0.80 \leqslant x < 0.85$, only a transport anomaly occurs at $T_{c2} \simeq 170$ K, and for $0.85 \leqslant x \leqslant 0.90$, no anomaly exists there. The magnetic properties for $0.80 \leqslant x \leqslant 0.90$ are understood in terms of a one-dimensional Heisenberg-like model with the V–O–V molecular orbital. In the crossover region between the spin-gap state and the linear-chain state, the paramagnetic phases without long-range order are stable down to low temperatures.

The properties for $0.47 \leqslant x \leqslant 0.496$ of the Tl system are similar to each other taking account of oxygen concentrations. $Tl_{0.479}V_2O_5$ has two crystallographically independent V ions with valences close to the average value and Tl ions without site randomness. All of the compositions exhibit the hopping conduction of negative small polarons and they have singlet properties with $J = 56$–81, $J' = 599$–638 and $J'' = 244$–276 K at the high-temperature side as expected in the trellis-layer model, where the ranges of J, J' and J'' come from a slight difference of the compositions. The phase transition takes place at about 150 K with changes of the superexchange coupling constants and the carrier-creation energies which may be related to the structural modification possibly due to the ordering of deficient Tl ions and/or the electron–phonon-coupling.

As described before, the nearly $\frac{1}{6}$-filled Ag compound with site randomness of Ag ions has the singlet state in the low-temperature phase and the nearly $\frac{1}{8}$-filled Tl compound without site randomness of Tl ions is already in the singlet state at temperatures above room temperature. Therefore, it is suggested that the V_2O_5 layer structure of the $\frac{1}{6}$-filled Ag compound below the transition temperature is close to that of the Tl compound. It is also pointed out that the $(1/2n)$-filled trellis layer with integer n and in-plane wavefunctions has singlet properties. Thus it may be important to consider the intersite correlation energy as well as a polaronic nature of electrons inherent to 3d transition-metal oxides, in addition to an on-site correlation energy. It has recently been found that this model is also applicable to the singlet transition of V_6O_{13} [19].

Given the background described above, this work is aimed at other compounds of the δ-phase bronzes $Na_{0.56}V_2O_5$ and $Sr_{0.5}V_2O_5$, their average valences of V ions corresponding to 4.72 and 4.5 (apparently quarter-filled), respectively. The crystal structures projected on the ab-plane are shown in figure 1 [20, 21]. Here, the structure of $Na_{0.56}V_2O_5$ with monoclinic lattice constants of $a = 11.663$, $b = 3.6532$, $c = 8.92$ Å and $\beta = 90.91°$ is similar to that of the Ag compound. The Na ions have site randomness and an occupancy probability 0.56. On the other hand, $Sr_{0.5}V_2O_5$ is triclinic with lattice constants of $a = 23.536$, $b = 7.3985$, $c = 8.801$ Å, $\alpha = 89.989°$, $\beta = 88.28°$ and $\gamma = 90.029°$, corresponding to the doublings of a and b for the above cell. This superstructure is due to the perfectly ordered arrangement of Sr as shown in figure 1(b). Of the four crystallographically independent V sites, V1a and V2a are close to V^{5+}, while V1b and V2b are like V^{4+} [21]. In this work, the structural, transport and magnetic properties for these compounds have been investigated by means of x-ray diffraction and through measurements of electrical resistivity, thermoelectric power, magnetization and electron spin resonance (ESR). The experimental methods are presented in section 2, and the results for the Na and Sr compounds are discussed in sections 3.1 and 3.2, respectively; section 4 is devoted to conclusions.

2. Experiments

Polycrystalline specimens of $Na_{0.56}V_2O_5(Sr_{0.5}V_2O_5)$ were prepared with the solid-state reaction method by heating appropriate mixtures of $NaVO_3(Sr_2V_2O_7)$, V_2O_3 and V_2O_5 (99.99% purity) sealed in quartz tubes in Ar atmosphere at 923 K for 12 (24) h, respectively. Here, V_2O_3, $NaVO_3$ and $Sr_2V_2O_7$ were made according to the procedures described in [22, 15].

---

[1] The Heisenberg Hamiltonian is defined as $H = \sum_{\langle i,j \rangle} J S_i \cdot S_j$, S_i being the spin operator at site i.

Table 1. The slow and fast cooling rates dT/dt (K min^{-1}) and the lowest temperatures T_L (K) for the measurements of x-ray diffraction, electrical resistivity, thermoelectric power, magnetic susceptibility and ESR for $Na_{0.56}V_2O_5$.

	Slow cooling		Fast cooling	
	dT/dt	T_L	dT/dt	T_L
X-ray diffraction	0.6	141	14	80
Electrical resistivity	0.2	107	2.5	122
Thermoelectric power	0.2	83	2.5	96
Magnetic susceptibility	0.2	4.2	30	4.2
ESR	—	—	18	4.2

The single crystals of $Na_{0.56}V_2O_5$ were obtained by the Bridgman method at 993 K with the use of nominal compound $Na_{0.6}V_2O_5$.

X-ray powder diffractions were performed in the temperature range from 80 to 300 K for the Na compound and at 300 K for the Sr one using a Rigaku RAD-IIC diffractometer with Cu Kα radiation. For the single crystals of the Na compound, the x-ray four-circle diffraction was performed at 297 K on a Rigaku AFC-7R diffractometer (custom-made) with graphite-monochromated Mo Kα radiation and a 18 kW rotating-anode generator in order to determine the precise chemical composition through the usual structure analysis. The four-terminal electrical resistivity and thermoelectric power were measured with a DC method at temperatures above 80 K. The magnetizations were measured at temperatures from 4.2 to 300 K by the Faraday method with a field of up to 1 T, and the magnetic susceptibility was deduced from the linear part of the magnetization–field (M–H) curve with a decreasing field. The ESR measurements were performed with a JEOL TE-200 spectrometer at an X-band frequency in the region between 4.2 and 300 K.

As will be described in the next section, the electronic properties for $Na_{0.56}V_2O_5$ depend on the cooling rate. The cooling conditions for various measurements are summarized in table 1.

3. Results and discussion

3.1. $Na_{0.56}V_2O_5$

3.1.1. Valence distribution. The specimens prepared are single phase; at room temperature, the polycrystals have the lattice constants $a = 11.671(2)$, $b = 3.6566(6)$, $c = 8.9016(9)$ Å and $\beta = 91.05(1)°$; and the single crystals indicate that $a = 11.668(2)$, $b = 3.6550(6)$, $c = 8.912(5)$ Å and $\beta = 91.07(3)°$. The Na concentration for the single crystals is 0.579(15), determined with the discrepancy factor of $R = 0.057$ for 976 unique reflections with $|F_o| \geqslant 3\sigma$, F_o and σ being the observed structure factor and its standard deviation, respectively, in the range $2\theta \leqslant 80°$ [23]. These results nearly agree with the previous ones [20], indicating that the nonstoichiometric composition with $Na_{0.56}V_2O_5$ is rather stable. As will be described later, the thermal variations for electronic properties of this compound significantly depend on the cooling condition. Figure 2 shows the temperature dependences of the lattice constants on heating for the slow cooled (SC) and fast cooled (FC) states listed in table 1. For both of the states, the a- and c-axes basically shrink with decreasing temperature due to the reduction of thermal oscillation for atoms, whereas β increases. For the FC condition, there seems to exist a step-like anomaly at around 210 K in particular for the β values. In contrast, the SC data change continuously, accompanied with relatively large standard deviations. These properties should be mainly attributed to the order–disorder effect of Na ions with a site randomness.
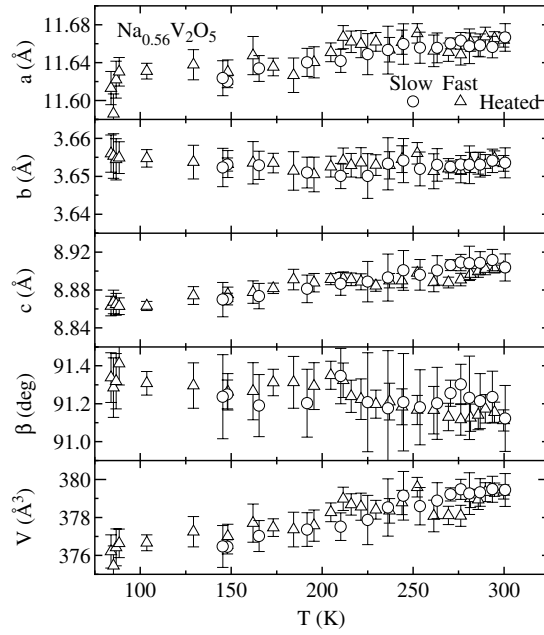
Figure 2. The temperature dependences of the lattice constants for polycrystalline specimens of Na$_{0.56}$V$_2$O$_5$ in the FC and SC conditions.

The bond-length–bond-strength analysis [24] based on the atomic parameters in [20] indicates that the valences of V1 and V2 are 4.75 and 4.61, respectively, which agree roughly with the average value expected from the chemical formula. The atomic parameters redetermined in this work provide valences of 4.73 and 4.68 for V1 and V2, respectively, both of which are almost equal to the average valence. Thus, Na$_{0.56}$V$_2$O$_5$ is near to the $\frac{1}{8}$-filled compound. Using the Hartree–Fock function for V^{4+} [25], the ground-state wavefunctions for the V1 and V2 are calculated to be $0.953d_{xy} - 0.302d_{yz}$ and $0.937d_{xy} - 0.349d_{yz}$, respectively, where $x \parallel a$ and $y \parallel b$. Both V1 and V2 have d_{xy}-type in-plane wavefunctions, so that the superexchange couplings at a similar z-level in the ab-plane are expected to be most effective. Thus, the double trellis-layer model is applicable to this system, as shown in figure 1(a), where the thick lines and the dotted lines denote the V–V paths at a similar z-level.

3.1.2. Transport properties. The in-plane electrical resistivities ρ for the single crystals as a function of the inverse temperature are shown in figure 3(a). Here, the full and open symbols indicate results for the cooled and heated processes, respectively; the circles and triangles are for the SC and FC conditions shown in table 1. All of the results basically exhibit nonmetallic conductions and the mobility at room temperature is 1.0×10^{-3} cm^2 V^{-1} s^{-1} for the carrier density 5.9×10^{21} cm^{-3}, which is classified into a small-polaron conduction in the framework of polaronic transports. The FC data indicate little thermal hysteresis and the energy gaps E_ρ empirically defined by

$$\rho = \rho_0 \exp(E_\rho/T), \tag{1}$$

where ρ_0 is assumed to be a constant, are different for high- and low-temperature regions. They are estimated to be 3.5×10^3 K above 270 K and 2.2×10^3 K below $T_{c\rho} \simeq 170$ K from the full and dotted lines, respectively. On the other hand, the SC results have a significant thermal
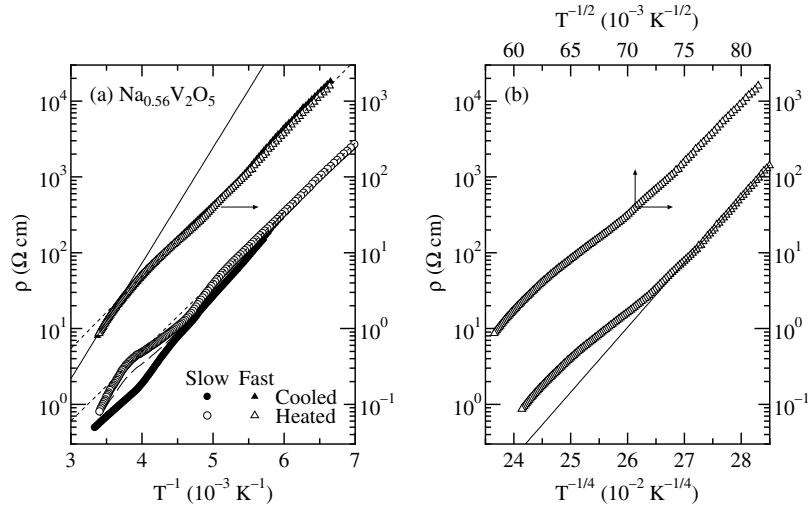
Figure 3. The temperature dependences of the in-plane electrical resistivities for single crystals of $Na_{0.56}V_2O_5$ in the SC and FC conditions: (a) ρ against T^{-1}, where the full and dotted lines indicate fits to equation (1); and (b) ρ against $T^{-1/4}$ (bottom abscissa) and $T^{-1/2}$ (top abscissa), where the full line is a fit to equation (2) with $d = 3$.

hysteresis above $T_{c\rho}$, indicating a first-order phase transition. The dotted line at the lower temperature provides $E_\rho = 2.1 \times 10^3$ K, which is comparable with the value below $T_{c\rho}$ for the FC state. A similar thermal hysteresis was observed for $Ag_xV_2O_5$ [16] and $Tl_xV_2O_5$ [17], although it was not significant for the nearly commensurate composition. Therefore, the first-order phase transition is a common property for the δ-phase bronzes with incommensurate monovalent M ions, which is attributed to the order–disorder effect of M. It is noted that the average values of the resistivities for the cooled and heated processes in the SC state agree well with the FC data, as indicated by the dashed curve in figure 3(a).

Considering the presence of nonstoichiometry or randomness of Na atoms, the Mott-type variable-range hopping (VRH) model [26] should also be examined:

$$\rho = \rho_0' \exp[(T_0/T)^{\frac{1}{d+1}}] \tag{2}$$

where ρ_0' is a constant, d is the dimensionality and T_0 corresponds to α^d/N, α and N indicating the envelope of the wavefunction as $\exp(-\alpha r)$ and the density of states for the hopping, respectively. On the basis of the FC data for the heated process against $T^{-1/4}$ ($d = 3$) and $T^{-1/2}$ ($d = 1$) plotted in figure 3(b), this model is found to be applicable at $T < T_{c\rho}$, although it is difficult to determine the dimensionality from the resistivity data alone owing to the narrow temperature region measured. The full line for the plot with $d = 3$ provides $T_0 = 1.5 \times 10^9$ K. When the energy range around the Fermi level for the 3d orbital distribution is smaller than 1 eV, the localization length α^{-1} is estimated to be smaller than 10^{-1} Å, which indicates a strong localization.

Figure 4(a) shows the in-plane thermoelectric power against the inverse temperature, where definitions on the symbols are the same as those for the resistivity. All of the data exhibit nonmetallic behaviours as expected from the resistivity data and they have negative values, suggesting electron carrier conduction. The FC data with the conditions given in table 1 have no thermal hysteresis, whereas the SC data exhibit a hysteresis at high temperatures. There exists a rapid change of the temperature variations at $T_{cS} \simeq 170$ K irrespective of the cooling rate. Here, T_{cS} agrees with $T_{c\rho}$ below which neither SC nor FC data for the resistivity have
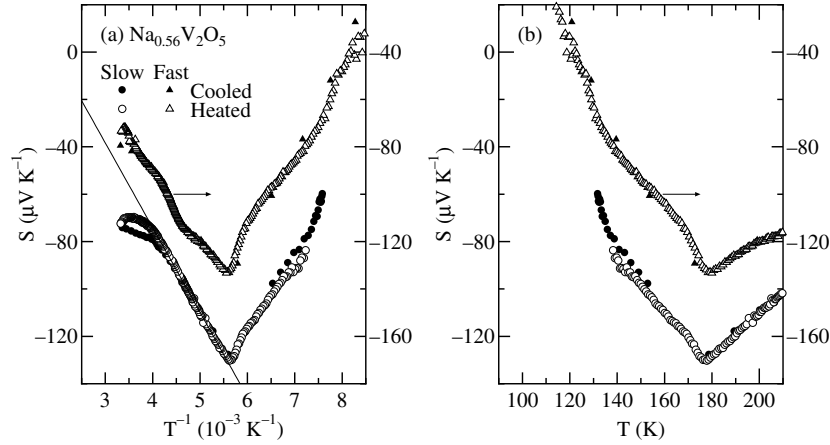
Figure 4. The temperature dependences of the in-plane thermoelectric powers for single crystals of Na$_{0.56}$V$_2$O$_5$ in the SC and FC conditions: (a) S against T^{-1}, where the full line shows a fit to equation (3); and (b) S against T at low temperatures.

thermal hysteresis. On the basis of the full line for $T > T_{cS}$ in figure 4(a), the temperature-independent value S_0 and the gap E_S empirically defined by

$$S = -eE_S/T + S_0 \tag{3}$$

are estimated to be 68.8(4) μV K^{-1} and 4.1×10^2 K, respectively. The significant difference between E_ρ and E_S may be characteristic of small-polaron motion if the VRH mechanism does not work there significantly. It is understood by considering the narrow tails of localized states which extend into the forbidden gap and a band of compensated levels originating from the Na doping near the middle of the gap. Thus, E_S in equation (3) corresponds to the width between the energies at the Fermi level and at the tail edge, and E_ρ in equation (1) is the sum of the energies for carrier creation and for hopping. On the other hand, the positive value of S_0 is not explained simply within the one-band model. Alternatively, it may be possible to see that the temperature dependence of the thermoelectric power around room temperature is not so large as the behaviour expected from the full line. In effect, the thermoelectric power for a nondegenerate gas [27],

$$S_H = \frac{k}{e} \ln \left(\frac{x}{2-x} \right) \tag{4}$$

where k is the Boltzmann coefficient, leads to $S_H = -81$ μV K^{-1} for $x = 0.56$, which is close to the room-temperature value. The low-temperature behaviours of the thermoelectric power are replotted in figure 4(b) in a linear scale. The data below T_{cS} do not have the temperature dependence expressed in equation (3), but seem to exhibit a positive power for T.

Let us consider the thermoelectric power in terms of the VRH model as discussed for the resistivity. It is known that a quasi-one-dimensional VRH with intrachain and interchain hopping qualitatively leads to a form of equation (3) [28], while two- and three-dimensional VRHs follow $S \propto T^{1/3}$ and $T^{1/2}$, respectively [29]. Thus, taking account of the resistivity results, it is suggested that the transport mechanism at low temperatures is of VRH type in three dimensions. On the other hand, the T^{-1}-like dependence of the thermoelectric power at high temperatures postulates the VRH transport in one dimension. The transition around $T_{c\rho}$ and T_{cS} may be related to the crossover of dimensionality for the VRH transport due to the change of the bandwidth in the transverse direction [28].
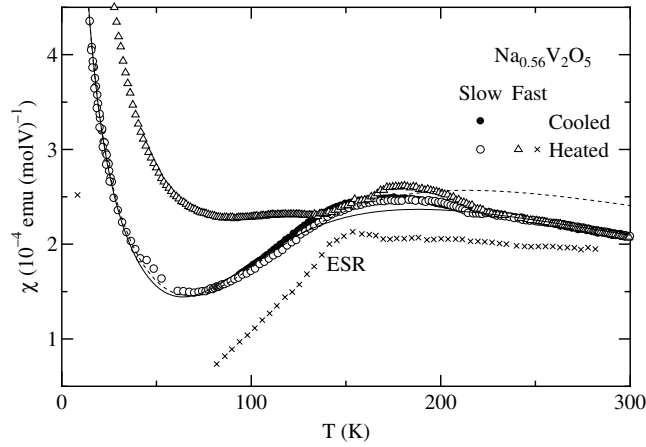
Figure 5. The temperature dependences of the magnetic susceptibilities for polycrystalline specimens of $Na_{0.56}V_2O_5$ in the SC and FC conditions and that of the ESR spin-susceptibility for single-crystal specimens in the FC condition. Here, the full and dotted curves indicate fits to equations (5)–(7).

In this section, the transport properties have been discussed with small-polaron and VRH models. At temperatures below $T_{c\rho}$ and T_{cS}, the latter model is plausible, while for the high-temperature region, further investigations are necessary in order to determine which of models is more appropriate.

3.1.3. Magnetic properties. The temperature dependences of the magnetic susceptibilities χ for the polycrystalline specimens in the FC and SC conditions (see table 1) are shown in figure 5. The SC data exhibit a small thermal hysteresis, in contrast to the transport properties. With decreasing temperature, the susceptibility increases with an upward curvature and exhibits a kink at $T_{c\chi 1} \simeq 210$ K; and then it exhibits a round maximum at $T_{c\chi 2} \simeq 170$ K that corresponds to $T_{c\rho}$ and T_{cS}. A Curie law-like increase of χ below 70 K may come from a phase such as a lattice imperfection or a magnetic impurity that cannot be detected by standard x-ray powder diffraction. Thus, the intrinsic spin-susceptibility tends to zero at low temperatures.

As described before, the trellis-layer model is applicable to this compound with superexchange couplings J, J' and J'' shown in figure 1(a). The susceptibility is described in the form

$$\chi = \chi_{\text{trellis}} + \chi_{\text{isolate}} + \chi_0, \tag{5}$$

$$\chi_{\text{isolate}} = \frac{C_{\text{isolate}}}{T + T_{\text{W}}^{\text{isolate}}}, \tag{6}$$

where χ_{trellis} is the susceptibility calculated by quantum Monte Carlo simulations for the trellis layer with intrinsic Curie constant C and three kinds of exchange couplings [18]; χ_{isolate} is the Curie–Weiss-type susceptibility of the isolated V^{4+} ions with parameters of C_{isolate} and the Weiss temperature $T_{\text{W}}^{\text{isolate}}$; and χ_0 corresponds to the temperature-independent susceptibility of the Van Vleck orbital and diamagnetic components. The fit to the data indicates J and J'' with large standard deviations to be significantly smaller than J'. In effect, a similar fit is obtained

with J' alone; that is, a dimer model χ_{dimer} instead of χ_{trellis} in equation (5) [3]:

$$\chi_{\text{dimer}} = \frac{4C}{T\left[\exp(J'/T) + 3\right]} \tag{7}$$

where J' is equal to the singlet–triplet excitation gap for the rung dimer. On the basis of the SC data above $T_{c\chi 1}$ with a small kink and below $T_{c\chi 2}$, the full curve in figure 5 is obtained, where $C = 0.080(1)$, $C_{\text{isolate}} = 0.0072(1)$ emu K (mol V)$^{-1}$, $J' = 337(1)$ K, $T_W^{\text{isolate}} = 2.1(1)$ K and $\chi_0 = 1.0(2) \times 10^{-5}$ emu (mol V)$^{-1}$. The overall agreement between the experimental and calculated results is satisfactory and the Curie constants described here are roughly consistent with the value expected from the chemical formula; $C_f = 0.10$ emu K (mol V)$^{-1}$ with the average g-factor of 1.96 described later. Between $T_{c\chi 1}$ and $T_{c\chi 2}$, the size of J' should be modified slightly. On the other hand, considering that the spin-singlet transition takes place at $T_{c\chi 2}$, the fit shown by the dotted curve in figure 5 is obtained with a Curie constant that agrees well with C_f. In this case, the ESR relaxation anomalies originated from the spin-singlet transition would be expected at $T_{c\chi 2}$, but this is not the case, as will be described later.

While the FC data at temperatures between $T_{c\chi 1}$ and 300 K are similar to the SC data, a significant difference exists below $T_{c\chi 1}$. The FC data have a large kink at $T_{c\chi 1}$ and a peak at temperature slightly higher than $T_{c\chi 2}$, and they are nearly temperature independent down to 70 K, and then increase significantly with decreasing temperature. In the next section, it is shown that this behaviour may be related to blocking phenomena of the superparamagnetic state.

3.1.4. ESR. The ESR signals measured in the heating process for the FC condition in table 1 are expressed by single and symmetric Lorentzians at temperatures below 8 K and above 80 K. Between 8 and 80 K, multisignals are observed for certain directions of the external field, which is sample dependent. The results presented here are for the single Lorentzians. The temperature dependence of the spin susceptibility estimated from the integrated intensity of the signal is shown in figure 5. It roughly corresponds to the SC result for the magnetic susceptibility taking account of the constant susceptibility χ_0. Thus, the FC effect observed for the magnetic susceptibility does not appear in the ESR susceptibility. In other words, the anomaly of the magnetic susceptibility for the FC condition is owing to the measurement time, for which typical values are 10^2 s for the Faraday method and the inverse of the measurement frequency 10^{-10} s for the ESR. This may be related to the blocking temperature in superparamagnetism for a system composed of fine magnetic particles [30]. In the present compound, the energy barrier preventing a spin direction from reversing is induced by the disordered effect of Na ions.

The angular dependences of the g-factors and the peak-to-peak linewidths W of ESR absorption derivatives are shown in figure 6(a) for the bc^*-plane and in figure 6(b) for the ab-plane. The temperature dependences of $g_{b(c^*)}$ and $W_{b(c^*)}$ are shown in figures 7(a) and (b), respectively. The g-factor has the following angular dependence:

$$g = (g_a^2 \cos^2\phi \sin^2\theta + g_b^2 \sin^2\phi \sin^2\theta + g_{c^*}^2 \cos^2\theta)^{1/2} \tag{8}$$

where θ and ϕ are the polar and azimuthal angles of the direction of the external field, respectively, with respect to the crystallographic axes (a, b, and c^*) which correspond to the principal axes (X, Y and Z). From figure 6, g_b depends on the direction of H_1; at 282 K, $g_b = 1.975$ with $H_1 \parallel a$ and $g_b = 1.965$ with $H_1 \parallel c^*$. However, g_b with $H_1 \parallel c^*$ increases with decreasing temperature and it becomes constant, about 1.98, below 210 K. Although the H_1-direction dependence of the g-factor due to the effect of nondiagonal dynamical susceptibility appears in a certain one-dimensional spin system [31, 15], this is not the case here. Alternatively, it may be related to the thermal hysteresis of Na order caused by a slight difference between the FC conditions. Then, for g_b, let us use the average value for $H_1 \parallel a$ and $H_1 \parallel c^*$.
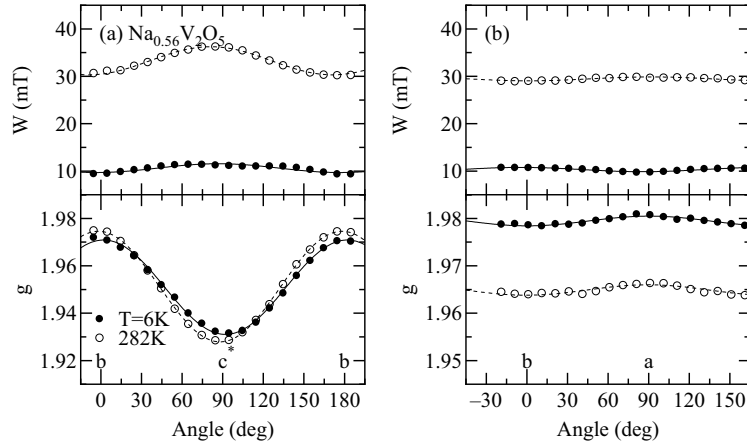
Figure 6. The angular dependences of the g-factors and the peak-to-peak linewidths of ESR absorption derivatives for $Na_{0.56}V_2O_5$ in (a) the bc^*- and (b) ab-planes in the FC condition. Here, the curves for g and the linewidths express fits to equations (8) and (10), respectively.
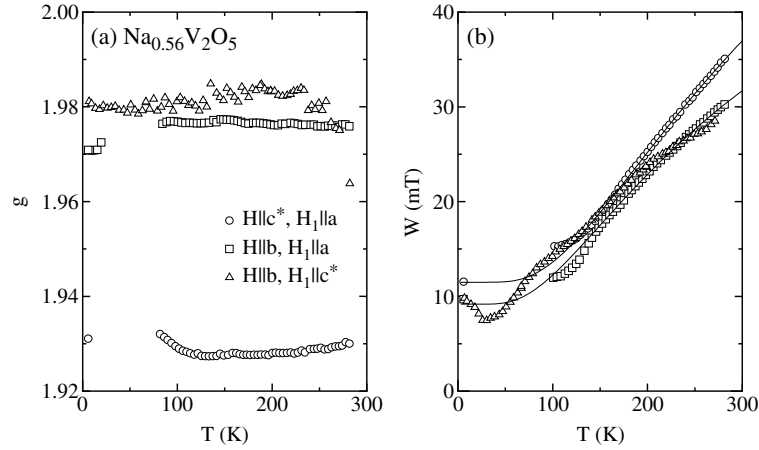

Figure 7. The temperature dependences of (a) the g-factors and (b) the peak-to-peak linewidths of ESR absorption derivatives for $Na_{0.56}V_2O_5$ for the heated process in the FC condition. Here the full curves are fits to equation (11).

The relation $g_a \simeq g_b > g_{c^*}$ is consistent with the d_{xy}-type ground-state wavefunction expected from the crystal-field analysis. The energy level configuration for V^{4+} may be calculated in terms of simple perturbation theory of the spin–orbit coupling [32]:

$$\Delta g_i = 2\lambda \sum_n \frac{|\langle n|L_i|0\rangle|^2}{E_n - E_0} \tag{9}$$

where $\Delta g_i = 2 - g_i$; λ is the spin–orbit coupling constant, L_i is the orbital angular momentum operator, and E_n is the energy of the orbital state n. With $|0\rangle = d_{xy}$, the energies corresponding to the d_{zx}, d_{yz} and $d_{x^2-y^2}$ states at 282 K are determined to be 55λ, 60λ and 108λ, respectively. The first excited state is close to being doubly degenerate.

The angular dependence of W is written as

$$W = W_a \cos^2\phi \sin^2\theta + W_b \sin^2\phi \sin^2\theta + W_{c^*} \cos^2\theta \tag{10}$$

with the same definitions for θ and ϕ as in equation (8) and with $W_a \simeq W_b$. The W-values are found to be significantly correlated with the Δg-values; that is, the maximum and minimum of W correspond to those of $|\Delta g|$, respectively. Although for the linewidth in the strongly exchange-coupled system there have been considered to exist several origins, such as the dipole–dipole interaction, the anisotropic exchange interaction and the Dzyaloshinsky–Moriya antisymmetric exchange interaction [17], the recent field theory indicates the quantitative estimation of the linewidth to be difficult [33].

With decreasing temperature, the linewidth decreases monotonically, and at low temperatures, it seems to become constant. Since the present ESR signals mainly come from the spins excited thermally from the rung dimer, they are expected to disappear at low temperatures. However, signals with g-factors similar to those at high temperatures are clearly observed. This is a contribution from the isolated spins that reside in a imperfect lattice of the crystal, judging from the ESR susceptibility. In this case, cross-relaxation likely occurs between isolated ions and dimers. Assuming that the isolated ion cross-relaxes to a triad consisting of a dimer with one more loosely coupled third ion, the temperature dependence of the linewidth in the region $T \ll J'$ under the extreme narrowing condition is written as [34]

$$W \propto \exp(-J'/T). \tag{11}$$

Applications of this equation to the data for W_{c^*} and W_b provide $J' = 372(2)$ and $298(1)$ K, respectively, as shown by the full curves in figure 7(b). These values agree roughly with the values obtained from the analysis of magnetic susceptibility. The validity of this relaxation model should be checked through the direct measurement of spin-lattice relaxation times for V ions.

3.2. $Sr_{0.5}V_2O_5$

3.2.1. Valence distribution. The polycrystalline specimens obtained are single phase, having a triclinic cell with $a = 23.529(1)$, $b = 7.3987(8)$, $c = 8.7894(5)$ Å, $\alpha = 89.965(9)°$, $\beta = 88.325(7)°$ and $\gamma = 89.984(7)°$, which correspond roughly to the previous data [21]. On the basis of the bond-length–bond-strength relation [24], the valences for V1a, V1b, V2a and V2b ions are estimated to be 4.80(1), 4.12(1), 4.86(1) and 4.20(1), respectively, which indicates order like V^{4+} and V^{5+} more clearly as compared with the previous result [21]. Thus $Sr_{0.5}V_2O_5$ is roughly regarded as being $\frac{1}{2}$-filled. The valence distribution pattern is drawn in figure 1(b). The ground-state wavefunctions for each V site are approximately described as: for V1a, $-0.883d_{xy} + 0.453d_{yz}$; for V2a, $0.832d_{xy} + 0.551d_{yz}$; for V1b, $0.938d_{xy} - 0.324d_{yz}$; and for V2b, $-0.899d_{xy} - 0.436d_{yz}$, where $z \parallel c$ and $y \perp c$ in the bc-plane. Since both of the V^{4+}-like sites have d_{xy}-type in-plane wavefunctions, the superexchange couplings at a similar z-level in the ab-plane may be most effective, as in the case of δ-$M_xV_2O_5$ with a uniform valence distribution. The valence order in this compound suggests transport in quasi-one dimension. The exchange coupling J_1 for the V1b–V2b path in the intralayer may be important, as shown in figure 1(b). The sign of J_1 is known to depend sensitively on the local nature of wavefunctions for V and O ions [8, 35]. Finite exchange couplings J_2 for V2b–V2b and J_3 for V1b–V1b in the interlayers are also expected, since in the molecular field approximation their sizes should be proportional to the square of electron concentration. Thus, there exists the alternating-exchange chain of $-J_2-J_1-J_3-J_1-J_2-$ for the $a + 2b$ direction, as shown in figure 1(b) by the thick lines.

3.2.2. Transport properties. The electrical resistivity and the thermoelectric power for the polycrystalline specimens as a function of the inverse temperature are shown in figure 8. Both sets of data exhibit a semiconducting conduction without a thermal hysteresis. The
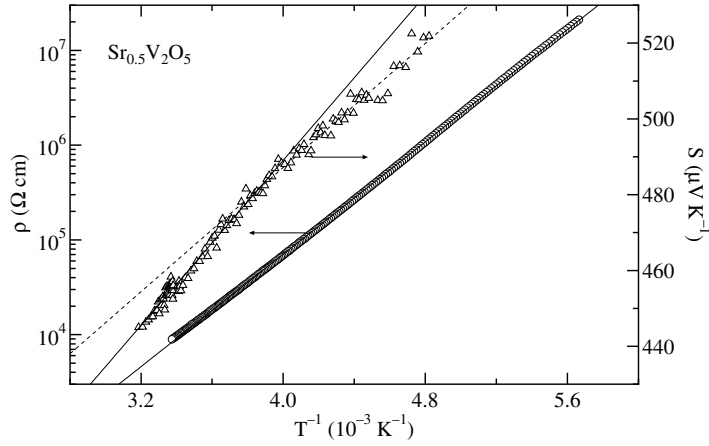
Figure 8. The temperature dependences of the electrical resistivity and the thermoelectric power for polycrystalline specimens of $Sr_{0.5}V_2O_5$. Here, the full line for the resistivity indicates a fit to equation (1) and the lines for the thermoelectric power are fits to equation (3).

full line for the resistivity in this figure indicates the activation energy in equation (1) to be $E_\rho = 3.4 \times 10^3$ K. The positive sign of the thermoelectric power shows a hole conduction, and the temperature dependences above and below 270 K are characterized with apparent gaps $E_S = 6.3(1) \times 10^2$ and $4.6(1) \times 10^2$ K in equation (3), as shown by the full and dotted lines, respectively. Both the semiconducting properties and the significantly large resistivities for the half-filled system suggest the electrons to be strongly correlated.

Theoretical investigations for the thermoelectric power in the one-dimensional Hubbard model indicate that approaching half-filling, S is hole-like and can become large for $U \gg t$, U and t being the Coulomb repulsion energy and the transfer matrix element, respectively, and it exhibits little thermal variation in a large temperature range [36]. It is also noted that the thermoelectric power with a half-filling is zero due to the particle–hole symmetry of the model. Therefore, assuming a slight deviation from half-filling, the present results with apparently small gap E_S at high temperatures may be understood in the framework of the Hubbard model.

3.2.3. Magnetic properties. The temperature dependence of the magnetic susceptibility for the polycrystalline specimen is shown in figure 9. As the temperature is lowered from the high-temperature side, the susceptibility increases and shows a maximum at about 110 K, and then it decreases significantly. The upturn of susceptibility below 20 K may be originated from isolated spins and thus the intrinsic spin susceptibility should go to zero. This singlet state should be attributed to the effect for a one-dimensional alternating-exchange chain formed by the V^{4+}-like pairs due to the valence order as pointed out before. Assuming that, for the interlayer exchange couplings, $J_2 \simeq J_3$ for simplicity, the susceptibility data are expressed in terms of the usual alternating-exchange chain model [37]:

$$\chi = \chi_{\text{alter}} + \chi_{\text{isolate}} + \chi_0 \qquad (12)$$

where χ_{alter} is calculated by quantum Monte Carlo simulations for the alternating-exchange chain with parameters C, J_1 and α, α being J_2/J_1. As indicated by the full curve in figure 9, all of the data are well explained by the following parameters: $C = 0.1586(3)$ emu K (mol V)$^{-1}$, $J_1 = 191.0(2)$ K, $\alpha = 0.573(1)$, $C_{\text{isolate}} = 2.95(3) \times 10^{-3}$ emu K (mol V)$^{-1}$ and $T_W^{\text{isolate}} = 4.6(1)$ K. From these parameters, the energy gap
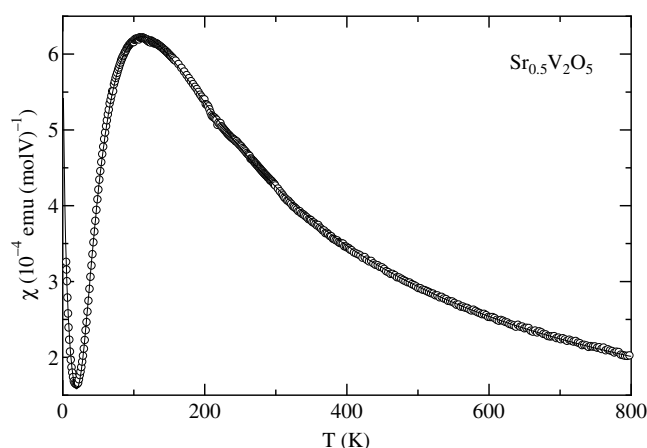
Figure 9. The temperature dependence of the magnetic susceptibility for the polycrystalline specimen of Sr$_{0.5}$V$_2$O$_5$, where the full curve shows a fit to equation (12).

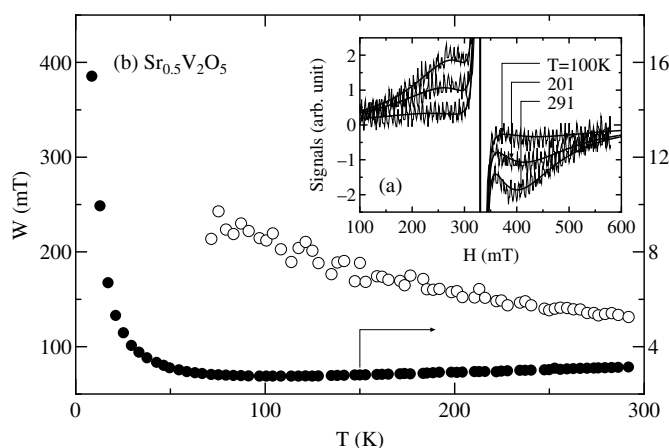**Figure 10.** (a) ESR signals for the polycrystalline specimen of Sr$_{0.5}$V$_2$O$_5$ at several temperatures, where the smooth curves represent the calculated results with symmetric Lorentzian line shape; and (b) the temperature dependences of the peak-to-peak linewidths for the intrinsic and extrinsic signals.

occurring at wavevector $q = 0$ and π is determined to be $\Delta_{\text{alter}} \simeq 113$ K. The Curie constant corresponds to that estimated on the basis of the chemical formula with the ESR g described below; $C_{\text{f}} = 0.17$ emu K (mol V)$^{-1}$.

3.2.4. ESR. The ESR signals consist of two kinds of symmetric Lorentzians with large and small linewidths, as shown in figure 10(a). They are attributed to the intrinsic signal and the extrinsic contribution from lattice imperfections or impurities, respectively, since the intensity for the large width at 292 K is about 20 times larger than that for the small width and its temperature dependence qualitatively corresponds to that for the magnetic susceptibility shown in figure 9. The intrinsic signals are observed above 70 K, below which the apparent intensity for another signal restricts the resolution of the spectrometer. There is no distortion of the line shape within experimental error. The analysis for the intrinsic signal is finally performed with

assumption of temperature-independent $g = 1.91$, since it provides fits close to those when g varies with temperature.

The temperature dependences of the peak-to-peak linewidths W_{in} and W_{ex}, corresponding to the intrinsic and extrinsic signals, respectively, are shown in figure 10(b). With decreasing temperature, W_{in} increases gradually, which may be caused by short-range fluctuations of the staggered magnetization [38]. This behaviour is also similar to the field-theoretical prediction in the presence of a staggered field for the $S = 1/2$ antiferromagnetic chain [33]. It is noted that for the lattice-dimerized phase in the one-dimensional antiferromagnetic compound $CuGeO_3$, the ESR linewidth becomes narrow with decreasing temperature at temperatures well below the spin–Peierls transition [39]. Unfortunately, it is difficult to observe the intrinsic signal for $Sr_{0.5}V_2O_5$ at $T \ll J_1, J_2$ owing to the presence of sharp impurity signals as mentioned before.

4. Conclusions

For the double trellis-layer bronzes $M_xV_2O_5$, the structural, transport and magnetic properties of $Na_{0.56}V_2O_5$ and $Sr_{0.5}V_2O_5$ have been investigated. The bond-length–bond-strength relation suggests that the effective valences of two independent V ions for the Na compound are similar to each other, and thus the d electrons are distributed uniformly. On the other hand, for the Sr compound that has a superstructure due to the complete order of Sr, valence order like V^{4+} and V^{5+} appears. The crystal-field analyses indicate that the ground-state wavefunctions of the V ions are mainly in-plane-type for both of the compounds. For the uniform valence distribution, the superexchange coupling between the V ions within a trellis layer is the most effective, as in the case of δ-$M_xV_2O_5$ with M = Ag and Tl.

The electronic properties of $Na_{0.56}V_2O_5$ depend on the cooling rate, which is likely due to the configuration for the order of Na. The lattice constants against temperature also reflect this anomaly. Here, the slow and fast cooling conditions roughly correspond to the rates below and above 1 K min^{-1}, respectively. The electronic transports at low temperatures are of VRH conduction in three dimensions, while those at high temperatures are characterized as negative small-polaron motion or VRH in one dimension. The slow cooling gives rise to the spin-singlet state due to the large exchange coupling for the rung in the trellis layer, which is consistent with our model that the $(1/2n)$-filled trellis layer with integer n and in-plane wavefunctions gives rise to a gap. On the other hand, fast cooling leads to a metastable state depending on the time of measurement; the static susceptibility follows a Curie law with large constant susceptibility and the intrinsic susceptibility obtained from the ESR decreases significantly as the temperature is lowered. This may be induced by the disordered effect of Na ions. In order to reveal the metastable state, further experiments are needed. The energy level configuration for V ions are determined and the ESR relaxation is discussed in the framework of cross-relaxation.

$Sr_{0.5}V_2O_5$ has an alternating-exchange (half-filled) chain due to the valence order of V^{4+} and V^{5+}. The electronic transports are close to those of an insulator, which is due to the electron correlation. The singlet state is understood with the alternating-exchange couplings of $J_1 = 191$ K and $J_2 = 109$ K with $\Delta_{alter} \simeq 113$ K. The ESR result at $T \gtrsim \Delta_{alter}$ is qualitatively consistent with the scenario in the presence of a staggered field for the $S = 1/2$ antiferromagnetic chain.

References

[1] Bouloux J C and Galy J 1973 *Acta Crystallogr.* B **29** 1335
[2] Bouloux J C and Galy J 1973 *Acta Crystallogr.* B **29** 269
[3] Onoda M and Nishiguchi N 1996 *J. Solid State Chem.* **127** 359

[4] Onoda M and Ohyama A 1998 *J. Phys.: Condens. Matter* **10** 1229
[5] Kodama K, Harashina H, Sasaki H, Kobayashi Y, Kasai M, Taniguchi S, Yasui Y, Sato M, Kakurai K, Mori T and Nishi M 1997 *J. Phys. Soc. Japan* **66** 793 and references therein
[6] Fukumoto Y and Oguchi A 1998 *J. Phys. Soc. Japan* **67** 2205 and references therein
[7] Harashina H, Kodama K, Shamoto S, Taniguchi S, Nishikawa T, Sato M, Kakurai K and Nishi M 1996 *J. Phys. Soc. Japan* **65** 1570
[8] Nishiguchi N, Onoda M and Kubo K 2002 *J. Phys.: Condens. Matter* **14** 5731
[9] Smolinski H, Gros C, Weber W, Peuchert U, Roth G, Weiden M and Geibel C 1998 *Phys. Rev. Lett.* **80** 5164
[10] Meetsma A, de Boer J L, Damascelli A and Pastra T T M 1998 *Acta Crystallogr.* C **54** 1558
[11] von Schnering H G, Grin Y, Kaupp M, Somer M, Kremer R K, Jepsen O, Chatterji T and Weiden M 1998 *Z. Kristallogr.* **213** 246
[12] Horsch P and Mack F 1998 *Eur. Phys. J.* B **5** 367
[13] Isobe M and Ueda Y 1996 *J. Phys. Soc. Japan* **65** 1178
[14] For a review, Lemmens P, Güntherodt G and Gros C 2003 *Phys. Rep.* **375** 1
[15] Onoda M and Kagami T 1999 *J. Phys.: Condens. Matter* **11** 3475
[16] Onoda M and Arai R 2001 *J. Phys.: Condens. Matter* **13** 10399
[17] Onoda M and Hasegawa J 2002 *J. Phys.: Condens. Matter* **14** 5045
[18] Johnston D C, Troyer M, Miyahara S, Lidsky D, Ueda K, Azuma M, Hiroi Z, Takano M, Isobe M, Ueda Y, Korotin M A, Anisimov V I, Mahajan A V and Miller L L 2000 *Preprint* cond-mat/0001147
[19] Onoda M, Ohki T and Uchida Y 2004 *J. Phys.: Condens. Matter* **16** 7863
[20] Kanke Y, Kato K, Takayama-Muromachi E and Isobe M 1990 *Acta Crystallogr.* C **46** 536
[21] Kato K, Kanke Y, Oka Y and Yao T 1998 *Z. Kristallogr.* **213** 399
[22] Onoda M, Ohta H and Nagasawa H 1991 *Solid State Commun.* **79** 281
[23] teXsan 1992 *Crystal Structure Analysis Package* (Woodlands, TX: Molecular Structure Corporation)
[24] Zachariasen W H 1978 *J. Less-Common Met.* **62** 1
[25] Freeman A J and Watson R E 1965 *Magnetism* part A, vol 2, ed G T Rado and H Suhl (New York: Academic)
[26] Mott N F 1968 *J. Non-Cryst. Solids* **1** 1
[27] Heikes R R 1961 *Thermoelectricity* ed R R Heikes and R W Ure (New York: Interscience)
[28] Onoda M 2004 *J. Phys.: Condens. Matter* **16** 8957
[29] Brenig W, Döhler G H and Wölfle P 1973 *Z. Phys.* **258** 381
[30] See, for example Binder K and Young A P 1986 *Rev. Mod. Phys.* **58** 801
[31] Natsume Y, Sasagawa F, Toyoda M and Yamada I 1980 *J. Phys. Soc. Japan* **48** 50
[32] See, for example Abragam A and Bleaney B 1970 *Electron Paramagnetic Resonance of Transition Ions* (Oxford: Clarendon)
[33] Oshikawa M and Affleck I 2002 *Phys. Rev.* B **65** 134410
[34] Owen J and Harris E A 1972 *Electron Paramagnetic Resonance* ed S Geschwind (New York: Plenum)
[35] Onoda M and Nishiguchi N 1999 *J. Phys.: Condens. Matter* **11** 749
[36] Zemljiĉ M M and Prelovŝek P 2005 *Phys. Rev.* B **71** 085110 and references therein
[37] Johnston D C, Kremer R K, Troyer M, Wang X, Klümper A, Bud'ko S L, Panchula A F and Canfield P C 2000 *Phys. Rev.* B **61** 9558 and references therein
[38] Huber D L 1972 *Phys. Rev.* B **6** 3180
[39] Honda M, Shibata T, Kindo K, Sugai S, Takeuchi T and Hori H 1996 *J. Phys. Soc. Japan* **65** 691